This is a repository copy of *Viscoelastic Hele-Shaw flow in a cross-slot geometry*.

White Rose Research Online URL for this paper:
http://eprints.whiterose.ac.uk/128257/

Version: Published Version

Viscoelastic Hele-Shaw flow in a cross-slot geometry

S.T. Chaffin *, J.M. Rees

School of Mathematics and Statistics, University of Sheffield, Hicks Building, Hounsfield Road, Sheffield, S3 7RH, UK

ARTICLE INFO

ABSTRACT

In this paper a cross-slot geometry for which the height of the channel is small compared to the other channel dimensions is considered. The normal components of the viscoelastic stresses are found analytically for a second order fluid up to numerical inversion. The validity of the theoretical analysis was corroborated by comparison with numerical simulations based on a stabilized Galerkin least squares finite element method using an Oldroyd B fluid. Close agreement was found between numerical predictions and analytical results for Weissenberg numbers up to 0.2. An explicit expression is formulated for viscoelastic parameters in terms of the variation and strength of the first normal stress difference around the stagnation point. The analysis is generalized for the case where the inlet channel width is different from the outlet channel width. For such configurations it was found that uniformity of the elongation rate was reduced.

© 2017 The Authors. Published by Elsevier Masson SAS. This is an open access article under the CC BY license (http://creativecommons.org/licenses/by/4.0/).

1. Introduction

Polymer melts, which are widely used in processing operations such as injection molding, mixing and extrusion, exhibit non-Newtonian properties. Due to the relaxation times involved and memory effects, the ability to accurately predict the velocity and stress fields is still a challenging problem.

The modeling of such viscoelastic fluids has proven to be difficult, both numerically and analytically, even in the most simple of geometries. Analytical solutions are often presented under the assumption of constant velocity gradients, i.e. constant shear or elongation. Other solutions have been found, for example, an analytical solution for a FENE-P fluid was presented by Oliveira [1] and Rajagopal and Bhatnagar [2] found solutions for the flow of an Oldroyd B fluid, though exact analytical results often require the specification of a flow field such that the advection terms are zero. In this paper we use perturbation methods to derive a semi-analytical result for a second order fluid in a Hele-Shaw cross-slot device. The Hele-Shaw approximation necessitates that the geometry must have one length scale which is much smaller than the others. In our system the channel height is assumed to be much smaller than its width and thus the aspect ratio, δ, is small. This approximation has been used in numerous other studies, see for instance [3,4]. A sketch of the full three-dimensional system is

given in Fig. 1. Mathematically, the system reduces to the two-dimensional system shown in Fig. 2. Under the Hele-Shaw assumption one can perform an analysis of the stress under non-constant elongation. A finite element formulation for this flow configuration was also undertaken to consider the validity of the analytical results. As we are considering the case of a Hele-Shaw, cell this allows one to use a small-channel approximation. The small channel approximation imposes no-slip conditions on the vertical wall but permits slip boundary conditions on the horizontal walls. In reality there is a small layer close to the horizontal walls where the no-slip condition forces the velocity to drop to zero.

Experimental interest in the cross-slot geometry is focused on investigating the extensional behavior of polymers and is motivated by the strong elongational nature of the flow in a cross-slot device. Birefringence techniques used in conjunction with numerical studies of extensional flows have been used effectively to assess the validity of constitutive models, however, studies of polymer melts have highlighted some inconsistencies due to end effects and beam deflections [5]. Recently, Scoulages et al. [6,7] made three-dimensional birefringent measurements of flow in a lubricated cross-slot geometry in a study aimed at removing end effects. Achievement of this goal would lead to greater conformity with two-dimensional simulations without the compromise of using large aspect ratios. It may be possible to extend the results of this paper to a lubricated device without the need for small aspect ratios using the theory of Joesph [8,9].

The cross-slot device does not produce pure extensional behavior throughout the flow field and the aim of generating purely extensional flows still proves challenging. Haward et al. [10] used

---

* Corresponding author.
E-mail addresses: s.chaffin@sheffield.ac.uk (S.T. Chaffin), j.rees@sheffield.ac.uk (J.M. Rees).
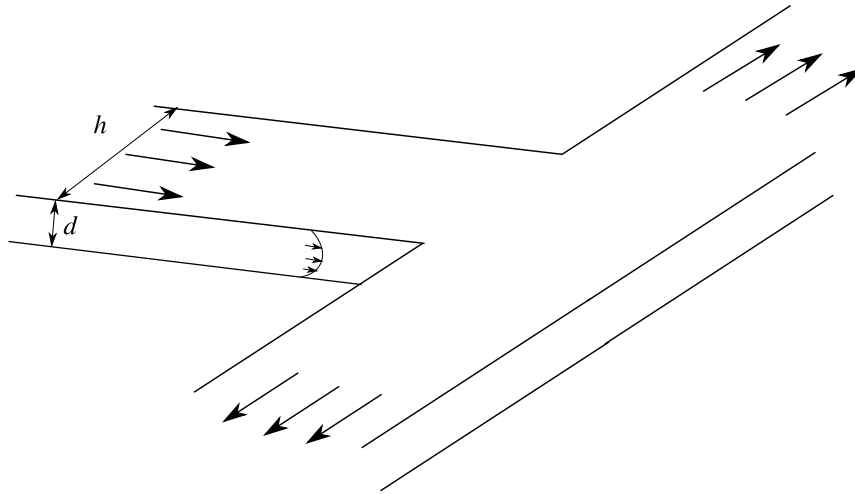
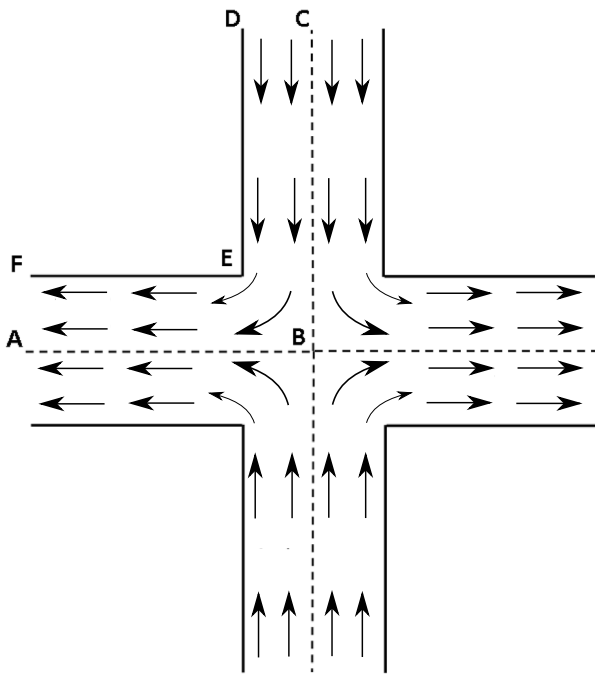**Fig. 1.** Sketch of the three-dimensional geometry.

Fig. 2. Two-dimensional slice of the cross-slot geometry. The widths of the inlet section of the channel DC and the outflow channel FA are taken to be equal in Section 4 and unequal in Section 5.

numerical simulations to optimize the shape of corner regions in a cross-slot to produce a more homogeneous extensional flow field. This study was purely two-dimensional which can be difficult to realize experimentally due to end effects which arise from finite aspect ratios.

The cross-slot device also exhibits strong bifurcating behavior with visco-elastic fluids [5,11–13]. Sousa et al. [14] considered the effects of aspect ratio on this instability. They found that for smaller aspect ratios the symmetry breaking bifurcation required a larger Weissenberg number (W_e), and that for sufficiently small aspect ratios, the symmetry breaking bifurcation was superseded by a transient bifurcation. Cruz et al. [15] performed computational investigations using a PTT fluid model. Cruz et al. reported the same behavior as Sousa et al. [14], finding that the unstable flow regimes are along the diagonals of the cross-slot. Such instabilities

will not be considered in this study as we will assume symmetry of the device throughout. Bifurcations in cross-slot channels are not limited to non-Newtonian fluids. Poole et al. [16] found symmetry breaking birefringence for strongly inertial flows for Newtonian fluids, though the behavior of this bifurcation is inherently different to those caused by viscoelastic effects.

The aim of this investigation is to determine whether one can obtain analytic results for a viscoelastic fluid in a cross-slot device. This would be advantageous as three-dimensional simulations of viscoelastic fluids can prove costly in terms of both time and computational power. Our approach builds on the previous studies of viscoelastic stresses that assume an idealized extensional flow field. A complete solution for constant elongation flow for the upper-convective Maxwell model was found by Cruz and Pinho [17], who further generalized the work of Thomases and Shelley [18]. Cruz and Pinho found the dependency of the smoothness and singularities of the pressure and stresses to the elongation rate and the Deborah number. Analysis of more complex viscoelastic models in pure extensional fields have also been performed, such as the Giesekus [19] and finite extensibility models [20,21]. The latter two investigations provide explicit expressions for the width of the bifurcation strand in terms of the viscoelastic parameters.

We will find later that our solution is not valid in the corner region. Viscoelastic effects in corner regions have been extensively studied. Analytical studies have addressed the dynamics of Oldroyd B and Upper Convective Maxwell (UCM) fluids flowing in a channel containing a sharp bend. Renardy [22] used a similarity solution for the stress stream function and found that the stresses scaled $\sim r^{-\frac{2}{3}}$ in the corner region, where r is the distance from the corner. This work was subsequently generalized by Rallison and Hinch [23] to encompass a range of channel bend angles, and by Evans [24] who investigated the downstream effects. We refer to these studies to address the local corner effects. However, in this study we will focus predominantly on the stress effects along the line of symmetry in the outflow channel (the line AB in Fig. 2), which is not in the vicinity of the corner.

The difficulty in generating formulations for analytical flows in such a geometry can be overcome by the use of complex potential theory, namely the Schwarz–Christoffel mapping (SCM) theorem. Taking advantage of the symmetry of the cross-slot device means that we need only consider one quadrant.

In this paper, a finite element model is used to assess the validity of an approximate analytical solution for the flow of an inertialess Oldroyd B fluid in a three-dimensional cross-slot. We
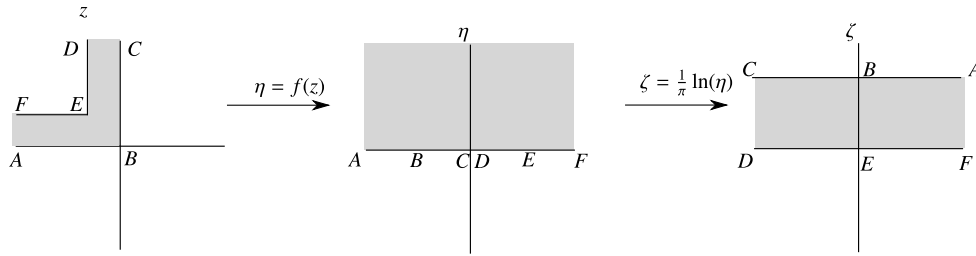
Fig. 3. Sketch demonstrating the conformal mapping. From left to right, mapping the z-plane onto the η-plane, and then the η-plane onto the ζ-plane.

found that this problem exhibited numerical difficulties arising from the sharp corner. The problem, as first noted by Keunings [25], is that increases in the mesh resolution led to poorer convergence at high W_e when a sharp corner is present. As one often needs high mesh resolution in such corner regions this proves problematic. However, Singh and Leal [26] noted that this poor convergence was due to insufficient mesh resolution in the azimuthal direction. We took note of this consideration in our numerical simulations.

In Section 2 we describe the construction of the flow field. The governing equations and flow field are presented in Section 3. For the case of inlet and outlet channels of equal width, the viscoelastic stress components and stagnation point pressure are analyzed in Section 4. The effects of varying the inlet and outlet channel width ratios are considered in Section 5. The conclusions are summarized in Section 6.

2. Construction of the flow field

Under the assumption of a small aspect ratio δ under zero Reynolds number for a Newtonian fluid, the mass and momentum conservation equations can be written as [27]

$$\mathbf{u}_{in} = -\frac{1}{2\mu}\bar{\nabla}px_3\left(d - x_3\right), \quad \frac{\partial p}{\partial x_3} = 0, \quad u_3 = 0, \quad \bar{\nabla}\cdot\mathbf{u}_{in} = 0, \tag{1}$$

except for a small region near the walls of order $\mathcal{O}(\delta)$ where the no-slip condition dominates. Here $\mathbf{u}_{in} = (u_1, u_2)$ is the in-plane velocity, x_1 and x_2 are the in-plane coordinates. Likewise, u_3 is the out-of-plane component of the velocity where x_3 is perpendicular to x_1 and x_2. The variable p denotes the pressure, $\bar{\nabla}$ is the in-plane gradient operator and d denotes the channel height. In a plane with x_3 fixed, this is analogous to the commonly used potential flow problems for irrotational fluids whereby $\mathbf{u}_{in} = \bar{\nabla}\phi$, where ϕ is the velocity potential which acts analogous to pressure in our problem.

Potential flow theory can be used to find a solution for the flow in complex channel geometries by superposing fundamental solutions, such as sinks, sources, dipoles, etc. It is often advantageous to work in terms of the complex potential, w, which is given by

$$w(z) = \phi + i\psi, \tag{2}$$

where z is the complex variable $x_1 + ix_2$, and ψ is the stream-function for the in-plane velocity (u_1, u_2). It is easily shown that the derivative of (2) can be used to find the velocity components (u_1, u_2) from

$$\frac{dw}{dz} = u_1 - iu_2. \tag{3}$$

To construct the flow field as in Fig. 2, we make use of the SCM theorem [28]. The SCM theorem concerns the conformal transformation of the upper half-plane onto the interior of a simple polygon. This theorem states that for n points along the real axis $(\eta_1, \eta_2, \ldots, \eta_n)$ corresponding to the vertices of a simple polygon, such that $\eta_1 < \eta_2 < \cdots < \eta_n$, where $\theta_1, \theta_2, \ldots, \theta_n$ are the internal

angles of the polygon, the transformation from the η-plane to the z-plane is given by

$$\frac{dz}{d\eta} = K(\eta - \eta_1)^{\frac{\theta_1}{\pi} - 1}(\eta - \eta_2)^{\frac{\theta_2}{\pi} - 1}\cdots(\eta - \eta_n)^{\frac{\theta_n}{\pi} - 1}, \tag{4}$$

where K is a complex constant. If one chooses a map from the corners of a channel containing a right-angled bend, as shown in Fig. 2, to the η-plane given by

$$A \rightarrow -\infty, \quad B \rightarrow -a, \quad C, D \rightarrow 0,$$
$$E \rightarrow b, \quad F \rightarrow +\infty, \tag{5}$$

then the SCM theorem gives

$$\frac{dz}{d\eta} = K\eta^{-1}(\eta + a)^{-\frac{1}{2}}(\eta - b)^{\frac{1}{2}}, \tag{6}$$

where a and b are positive non-zero real constants. Upon integration, it should be remembered that the constant of integration will be complex. Initially the SCM theorem maps the cross-slot geometry onto the upper half infinite plane. This semi-infinite half plane can then be readily mapped onto an infinitely long rectangle of unit height using the transformation

$$\zeta = \frac{1}{\pi}\ln(\eta). \tag{7}$$

These mappings are shown graphically in Fig. 3 which also depicts the mappings of the vertices. The complex stream function for a uniform flow with constant flux Q_0 from C, D to A, F, in the ζ-plane, is given by

$$w(\zeta) = Q_0\zeta, \tag{8}$$

which can be written as

$$w(\eta) = \frac{U_0h}{\pi}\ln(\eta), \tag{9}$$

where we have used the fact that for a channel of height h, and constant flow U_0 we can write $Q_0 = U_0h$. Physically, in the η-plane, the complex potential w is analogous to a source with flux Q_0 around the origin, or in the z-plane to a flux source located infinitely far up the x_2-axis.

Combining (6) and (9) gives

$$\frac{dw}{dz} = \frac{U_0h}{\pi K}\frac{\sqrt{(\eta + a)}}{\sqrt{(\eta - b)}}. \tag{10}$$

The constants are determined by imposing the condition of a uniform flow stream at the channel inlet and outlet. This gives rise to

$$\frac{dw}{dz} \sim -U_0 \quad \text{as} \quad \eta \rightarrow \pm\infty, \tag{11}$$

$$\frac{dw}{dz} \sim U_0i \quad \text{as} \quad \eta \rightarrow 0. \tag{12}$$

Constraints (11) and (12) can be used to determine the constants, giving

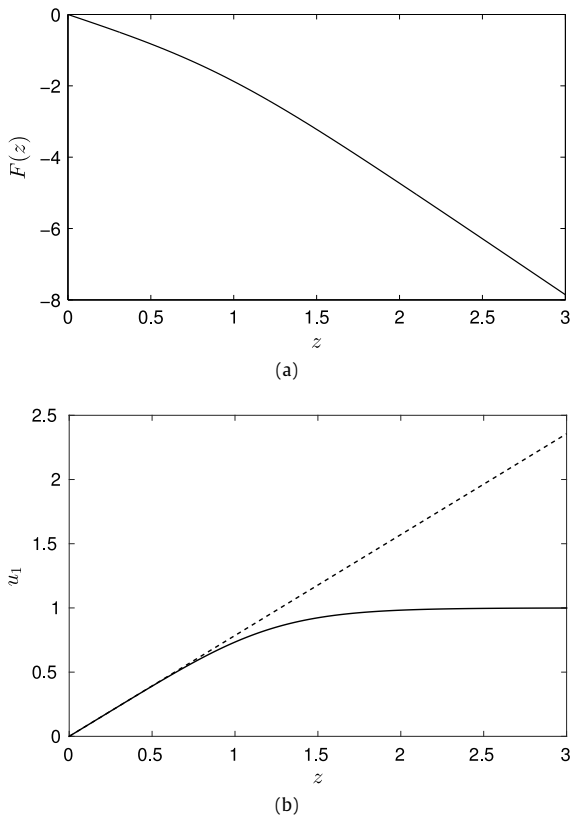$$K = -\frac{h}{\pi}, \quad a = b = 1. \tag{13}$$

Fig. 4. (a) The inverse function $F(z)$ plotted against its argument. (b) The predicted velocity along the line of symmetry (solid line) together with that predicted by assuming purely elongational flow (dashed line), plotted against z.

We note that there is an arbitrary degree of freedom for assigning the value of a and for convenience we set $a = 1$. By integrating (6) with the constants determined in (13) and making the substitution $\eta = \cosh(t)$ we find that

$$z(t) = -\frac{h}{\pi}\left(t + \tan^{-1}\left(\frac{1}{\sinh(t)}\right) - i\pi + \frac{\pi}{2}\right), \tag{14}$$

$$w(t) = \frac{U_0 h}{\pi}\ln\left(\cosh(t)\right), \tag{15}$$

where $t \in \mathbb{C}$ is a dummy variable. The constant of integration translates the geometry around the z-plane and is assigned such that the bottom corner is at the origin. Eqs. (14) and (15) form an implicit relation for the velocity field in the L bend geometry. Eq. (14) can be inverted to give the result, $t = F(z)$, which is plotted in Fig. 4 along with the velocity profile along the center line of the channel. The stream lines are shown in Fig. 5. Note that the solution gives rise to a singularity in the corner region which makes the flow unphysical in this vicinity. We can analyze the local behavior of the stagnation point by performing a Taylor expansion around $t = i\pi$. Ignoring the constant term, for w is unique up to an additive constant,

$$\begin{aligned} w &\sim \frac{U_0 h}{2\pi}(t - i\pi)^2 + \mathcal{O}(t - i\pi)^4, \\ z &\sim -\frac{2h}{\pi}(t - i\pi) + \mathcal{O}(t - i\pi)^2. \end{aligned} \tag{16}$$

We thus see that locally $w \sim \frac{U_0 \pi}{8h}z^2$, from which, by considering the imaginary component, we can recover the stagnation point stream-function $\psi = \frac{U_0 \pi}{4h}x_1 x_2$, used in previous studies of stagnation points, see for instance [18,29].
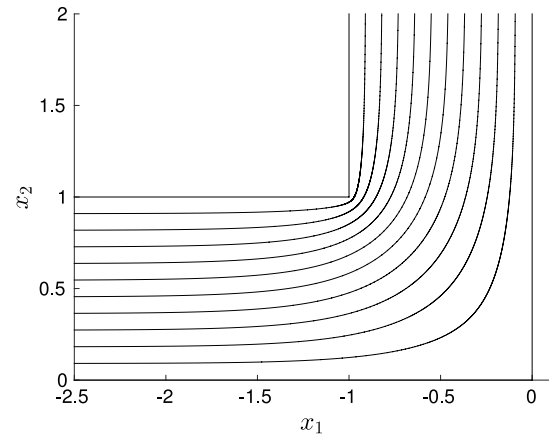

Fig. 5. Streamlines derived from the conformal mapping analysis.

The solution near the corner point E is mapped to $t = 0$. Taking the limit around $t = 0$, we have $z \sim hi - \frac{h}{6\pi}t^3$, $w \sim \frac{1}{2}t^2$, thus we are left with $w \sim 2^{-\frac{1}{3}}3^{\frac{2}{3}}\pi^{\frac{2}{3}}h^{-\frac{2}{3}}(z - z_0)^{\frac{2}{3}}$, i.e. locally one recovers $\phi \propto r^{\frac{2}{3}}\cos\left(\frac{2}{3}\theta\right)$, $\psi \propto r^{\frac{2}{3}}\sin\left(\frac{2}{3}\theta\right)$, which is the potential flow solution around a corner, as to be expected.

3. Governing equations

We will use the Newtonian velocity to try and capture viscoelastic effects. However to compare the validity of our approximation we will compare the result to the Oldroyd B equations coupled to the inertialess Navier stokes system

$$-\nabla p + \mu_s \nabla^2 \mathbf{u} + \nabla \cdot \boldsymbol{T} = \mathbf{0}, \quad \nabla \cdot \mathbf{u} = 0$$

$$\boldsymbol{T} + \lambda \overset{\triangledown}{\boldsymbol{T}} = \mu_p \dot{\boldsymbol{\gamma}}, \quad \dot{\boldsymbol{\gamma}} = \nabla\mathbf{u} + \nabla\mathbf{u}^T, \tag{17}$$

where here $\triangledown$ denotes the upper convective derivative. We chose the Oldroyd B model over the UCM because the addition of a small solvent viscosity can lead to considerably improved numerical stability [30]. However, one must bear in mind that the Oldroyd B model, in its relative simplicity, does predict physically unrealistic behavior at high elongation rates, notably, the well-known phenomenon of singular extensional viscosity at a finite elongation rate. Fundamentally, this problem arises as the Oldroyd B model has a linear extensional law at a microscopic scale. This is often overcome using models such as FENE-P, FENE-CR. Despite its limitations, the Oldroyd B model does reproduce complex viscoelastic behavior and is known to be a suitable choice for modeling Boger fluids [31]. Also, in general, most other more complex viscoelastic models reduce to the Oldroyd B model in certain parameter limits.

We will therefore solve the system of PDEs given by (17). The inlet velocity U and inlet width of the channel are taken to be of unity were the polymer and solvent viscosities are linked via $\mu_s + \mu_p = 1$. This is equivalent to the non-dimensionalization used by Craven [32].

We used the finite element software COMSOL Multiphysics. Numerical convergence can be difficult to achieve for the UCM and Oldroyd B models, especially for high Weissenberg numbers in the presence of large velocity gradients. Here we make use of the Galerkin least squares (GLS) method to stabilize the equations as originally proposed by Hughes et al. [33]. The scheme used here follows the procedure of Behr et al. [34] which was implemented in COMSOL by Craven et al. [32]. The GLS method is similar to the commonly used streamline up-wind Petrov–Galerkin method that is often used for integrating the Navier–Stokes equations,

where the standard weak form of the equations is augmented with additional stabilization terms:

$$
\begin{aligned}
&- \langle \nabla \cdot \mathbf{w}, p \rangle + \mu_1 \langle \dot{\boldsymbol{\gamma}}[\mathbf{w}], \dot{\boldsymbol{\gamma}}[\mathbf{u}] \rangle + \frac{1}{2} \langle \dot{\boldsymbol{\gamma}}[\mathbf{w}], \mathbf{T} \rangle + \langle q, \nabla \cdot \mathbf{u} \rangle \\
&+ \langle \mathbf{S}, \mathbf{T} \rangle + \lambda \left\langle \mathbf{S}, \overset{\triangledown}{\mathbf{T}} \right\rangle - \mu_2 \langle \mathbf{S}, \dot{\boldsymbol{\gamma}}[\mathbf{u}] \rangle + \sum_{elements} \tau_{mom} \langle \ \nabla q - \nabla \cdot \mathbf{S} \\
&- \mu_1 \nabla \cdot \dot{\boldsymbol{\gamma}}[\mathbf{w}], \ \nabla p - \nabla \cdot \mathbf{T} - \mu_1 \nabla \cdot \dot{\boldsymbol{\gamma}}[\mathbf{u}] \ \rangle \\
&+ \sum_{elements} \rho \tau_{cont} \langle \nabla \cdot \mathbf{w}, \nabla \cdot \mathbf{u} \rangle \\
&+ \sum_{elements} \tau_{cons} \left\langle \left[\mathbf{S} + \lambda \overset{\triangledown}{\mathbf{S}} - \mu_2 \dot{\boldsymbol{\gamma}}[\mathbf{w}] \right], \right. \\
&\left. \left[\mathbf{T} + \lambda \overset{\triangledown}{\mathbf{T}} - \mu_2 \dot{\boldsymbol{\gamma}}[\mathbf{u}] \right] \right\rangle,
\end{aligned}
\tag{18}
$$

under the convention $\dot{\boldsymbol{\gamma}}[\mathbf{g}] = \nabla \mathbf{g} + \nabla \mathbf{g}^T$. The terms τ_{cons}, τ_{mom}, τ_{cont} are the GLS parameters as defined as in [34]. Here $\mathbf{w}$, $\mathbf{S}$, q denote the test functions for the velocity field, extra stress tensor and the pressure field respectively. The test functions are taken to be Lagrange polynomials. It was found that the greatest stability could be achieved using cubic elements for the velocity field, and quadratic elements for the pressure field and for the extra stress tensor, though mixed elements are non-mandatory as the GLS formulation negates compatibility conditions on the order of the test functions. In the corner region, one would expect large velocity gradients which would give rise to a lack of convergence in the FEM model.

The grid used for this study was composed of a mixed triangular, quadrilateral mesh comprising 20 374 elements, which was then swept in the x_3 direction to form 5 mesh layers. The mesh was refined until the dependency of the solutions on the mesh size varied on the order 0.1%. Predictions of the flow fields within the cross-slot were obtained by solving Eq. (18) along with the boundary conditions. At the inlet uni-directional flow is imposed and solved numerically along with the stress field. Along the lines of symmetry we impose

$$
\mathbf{u} \cdot \mathbf{n} = 0, \quad (\boldsymbol{\sigma} \cdot \mathbf{n}) \cdot \mathbf{t} = 0.
\tag{19}
$$

Zero surface traction was imposed across the channel outlet, i.e.

$$
\boldsymbol{\sigma} \cdot \mathbf{n} = \mathbf{0}.
\tag{20}
$$

Here $\mathbf{n}$ and $\mathbf{t}$ are the normal and tangential vectors respectively.

4. Weak coupling expansion

Thus far we have derived the velocity for a Newtonian fluid and have not considered any non-Newtonian effects. Of course, if we can decouple the velocity field from the non-Newtonian stress the problem simplifies dramatically. Common approaches to decoupling the non-Newtonian stress use a second order fluid and apply the Giesekus Tanner (GT) theorem [35] to decouple the flow field. However, as the flow field is neither rectilinear nor planar we cannot directly use the GT theorem. There is, however, another limit which could be considered. Following the approach of Moore et al. [36] one can assume that the polymer viscosity μ_p is small in comparison to solvent viscosity. To be strictly rigorous one must use the dimensionless approach of [36], however, informally one can search for a solution in the form $u \sim u^{(0)} + \mu_p u^{(1)} + \cdots$, $p \sim p^{(0)} + \mu_p p^{(1)} + \cdots$, and $\mathbf{T} = \mu_p \mathbf{T}^{(0)} + \mu_p^2 \mathbf{T}^{(1)} + \cdots$. Substituting these series into (17) and taking leading order in μ_p gives

$$
- \nabla p^{(0)} + \nabla^2 \mathbf{u}^{(0)} = \mathbf{0}, \quad \nabla \cdot \mathbf{u}^{(0)} = 0,
\tag{21}
$$

$$
\mathbf{T}^{(0)} + \lambda \left(\left(\mathbf{u}^{(0)} \cdot \nabla \right) \mathbf{T}^{(0)} - \nabla \mathbf{u}^{(0)\,T} \mathbf{T}^{(0)} - \mathbf{T}^{(0)} \nabla \mathbf{u}^{(0)} \right) = \dot{\boldsymbol{\gamma}}^{(0)}.
\tag{22}
$$

To leading order the velocity field completely decouples from the extra stress $\mathbf{T}^{(0)}$. Hence we can use the expression (15) to obtain $\mathbf{u}^{(0)}$ and then solve Eq. (22) to obtain the extra stress. Unfortunately, the velocity field and gradients are only implicitly a function of spacial coordinates, as t cannot be easily inverted to give a function of z. We can, however, locally invert t as a function of z using the inverse power series to give

$$
t(z) \sim i\pi - \frac{\pi z}{2h} - \frac{\pi^3 z^3}{96h^3} + \frac{\pi^7 z^7}{143360h^7} + \mathcal{O}(z^9).
\tag{23}
$$

It can be shown numerically that this series has a radius of convergence of approximately $\frac{z}{h} < 1.42$. Similarly we can find expansions for the velocity and velocity gradient fields. In order to do so it is useful to note the following expressions, where $'$ denotes differentiation with respect to z:

$$
\begin{aligned}
w'(t) &= U_0 \frac{\sinh(t)}{(-\cosh(t) + 1)}, \\
w''(t) &= -\frac{U_0 \pi}{h} \frac{\cosh(t)}{(1 - \cosh(t))^2}.
\end{aligned}
\tag{24}
$$

Thus locally at $t = i\pi$ the velocity field and gradients can be written as

$$
\begin{aligned}
w'(t) &\sim U_0 \left(-\frac{1}{2}(t - i\pi) + \frac{1}{24}(t - i\pi)^3 - \frac{1}{240}(t - i\pi)^5 \right) \\
&\quad + \mathcal{O}\left((t - i\pi)^7 \right),
\end{aligned}
\tag{25}
$$

$$
\begin{aligned}
w''(t) &\sim \frac{U_0 \pi}{h} \left(\frac{1}{4} - \frac{1}{64}(t - i\pi)^4 + \frac{1}{192}(t - i\pi)^6 \right) \\
&\quad + \mathcal{O}\left((t - i\pi)^8 \right).
\end{aligned}
\tag{26}
$$

Eq. (25) has an infinite radius of convergence. However, due to the pole at $t = 0$, Eq. (26) has a radius of convergence of π. Combining with the local inversion (23) allows one to form a power series for the velocity and its gradient in terms of z explicitly:

$$
\begin{aligned}
w'(z) &= \frac{U_0 \pi z}{4h} - \frac{U_0 \pi^5 z^5}{1520h^5} + \mathcal{O}(z^9), \\
w''(z) &= \frac{U_0 \pi}{4h} - \frac{U_0 \pi^5 z^4}{304h^5} + \mathcal{O}(z^8).
\end{aligned}
\tag{27}
$$

It is important to note that the constitutive equation (22) is now hyperbolic and can be solved along any given streamline. The choice of streamline can considerably simplify the problem and allow one to focus on a point of physical interest. As cross-slot devices are not focused on shearing effects, we will consider the Oldroyd B fluid along the center plane $x_3 = \frac{d}{2}$, where, by the x_3 symmetry, we can deduce that $T_{13}^{(0)} = T_{23}^{(0)} = T_{33}^{(0)} = 0$. By design, the key area of interest is the extension occurring at the stagnation point. We thus further simplify the model by solving only along the center streamline which passes through the stagnation point. On this streamline symmetry enforces that $T_{12}^{(0)} = 0$ and along the outlet channel we are thus left with the simple decoupled ODEs for $T_{11}^{(0)}$, $T_{22}^{(0)}$:

$$
\begin{aligned}
w' \frac{dT_{11}^{(0)}}{dz} - \left(2w'' - \frac{1}{\lambda} \right) T_{11}^{(0)} - \frac{2}{\lambda} w'' &= 0, \\
w' \frac{dT_{22}^{(0)}}{dz} + \left(2w'' + \frac{1}{\lambda} \right) T_{22}^{(0)} + \frac{2}{\lambda} w'' &= 0.
\end{aligned}
\tag{28}
$$

One could integrate these equations numerically. However, we will continue with our search for an approximate analytic result. Let us assume regularity in $T_{11}^{(0)}$ and $T_{22}^{(0)}$, that is, that the stresses can be expressed locally around the stagnation point as $T_{11}^{(0)} \sim a_0 + a_1 z + \cdots$, $T_{22}^{(0)} \sim b_0 + b_1 z + b_2 z^2$. Using expressions (27) and (28), whilst requiring a consistent balance to $\mathcal{O}(1)$, leads to $a_0 = \frac{2\pi U_0}{2h - \pi \lambda U_0}$, $b_0 = -\frac{2\pi U_0}{\pi \lambda U_0 + \lambda^{-1}}$. We can continue this approach to

find that, to higher orders in z, the general solution can be written as

$$T_{11}^{(0)} = \frac{\pi U_0}{2h - \pi U_0 \lambda} + \frac{\pi^5 U_0 z^4}{128 \left(\pi^2 U_0^2 \lambda^2 - 4h^2\right) h^3}$$
$$+ \cdots + \text{homogeneous term}, \qquad (29)$$

$$T_{22}^{(0)} = -\frac{\pi U_0}{\pi U_0 \lambda + 2h} + \frac{\pi^5 U_0 z^4}{128 \left(3\pi U_0 \lambda + 2h\right) \left(\pi U_0 \lambda + 2h\right) h^3}$$
$$+ \cdots + \text{homogeneous term}. \qquad (30)$$

The homogeneous solutions to leading order in z behave as $C_{11} z^{2 - \frac{4h}{U_0 \pi \lambda}}$, $C_{22} z^{-2 - \frac{4h}{U_0 \pi \lambda}}$. In the Newtonian limit as $\lambda \to 0$ these terms become singular at the stagnation point which clearly is non-physical, thereby we set $C_{11} = C_{22} = 0$. The powers of these singularities are analogous to those found by Cruz and Pinho [17].

Although the above expansion is only valid locally around the stagnation point one can extend the series using the continuous fraction approximation, but we need to consider what form this approximation should take. From (15) we can see that $t \sim z$ and considering the Newtonian case, where $\boldsymbol{T} \propto w''$, the stresses decay exponentially as $z \to \infty$. One cannot expect a polynomial fraction to decay as quickly as this, however, we could achieve polynomial decay as $z \to \infty$. We also expect the stress to be monotonically decreasing in z. We thus search for a Padé approximate in the form P_8^1. After rescaling by μ_p we find that the approximate simplifies to

$$T_{11} = \frac{U_0 h^{-1} A_0}{A_1 \left(\frac{z}{h}\right)^8 + A_2 \left(\frac{z}{h}\right)^4 + A_3},$$
$$T_{22} = \frac{U_0 h^{-1} B_0}{B_1 \left(\frac{z}{h}\right)^8 + B_2 \left(\frac{z}{h}\right)^4 + B_3}, \qquad (31)$$

where the parameters for T_{11} are given by:

$A_0 = 163840 \mu_p \pi \left(3\pi \bar{\lambda} + 2\right) \left(\pi \bar{\lambda} + 2\right)^2$,
$A_1 = \pi^8 \left(\pi \bar{\lambda} - 2\right) \left(7\pi^2 \bar{\lambda}^2 - 8\pi \bar{\lambda} - 4\right)$,
$A_2 = -1280\pi^4 \left(\pi \bar{\lambda} - 2\right) \left(3\pi \bar{\lambda} + 2\right) \left(\pi \bar{\lambda} + 2\right)$,
$A_3 = -163840 \left(\pi \bar{\lambda} - 2\right) \left(3\pi \bar{\lambda} + 2\right) \left(\pi \bar{\lambda} + 2\right)^2$.

Here $\bar{\lambda}$ is the Weissenberg number $\frac{U_0 \lambda}{h}$. Similarly for T_{22},

$B_0 = 163840 \mu_p \pi \left(5\pi \bar{\lambda} + 2\right) \left(3\pi \bar{\lambda} + 2\right)$,
$B_1 = \pi^8 \left(\pi \bar{\lambda} + 2\right) \left(15\pi^2 \bar{\lambda}^2 - 16\pi \bar{\lambda} - 4\right)$,
$B_2 = -1280\pi^4 \left(5\pi \bar{\lambda} + 2\right) \left(3\pi \bar{\lambda} + 2\right) \left(\pi \bar{\lambda} + 2\right)$,
$B_3 = -163840 \left(\pi \bar{\lambda} + 2\right) \left(5\pi \bar{\lambda} + 2\right) \left(3\pi \bar{\lambda} + 2\right)^2$.

Although one is mainly interested in the predicted stress, one should note that the Padé approximations for the stress can be used to explicitly approximate the velocity field, instead of using the more cumbersome implicit description in Eq. (15). The velocity gradient can readily be obtained from consideration of the Newtonian case:

$$w''(z) \approx P_8^1 = f(z) = \frac{81920 U_0 \pi / h}{\left(\frac{\pi z}{h}\right)^8 + 1280 \left(\frac{\pi z}{h}\right)^4 + 327680}. \qquad (32)$$

We can integrate the above to give the expression for the velocity field:

$$w'(z) = 81920 U_0 \left\{ -\frac{1}{4(r_1 - r_2) r_1^{\frac{3}{4}}} \ln \left(\frac{\pi z + r_1^{\frac{1}{4}}}{r_1^{\frac{1}{4}} - \pi z} \right) \right.$$
$$+ \frac{1}{4(r_1 - r_2) r_2^{\frac{3}{4}}} \ln \left(\frac{\pi z + r_2^{\frac{1}{4}}}{r_2^{\frac{1}{4}} - \pi z} \right) +$$

$$- \frac{1}{2(r_1 - r_2) r_1^{\frac{3}{4}}} \tan^{-1} \left(\frac{\pi z}{r_1^{\frac{1}{4}}} \right)$$
$$\left. + \frac{1}{2(r_1 - r_2) r_2^{\frac{3}{4}}} \tan^{-1} \left(\frac{\pi z}{r_2^{\frac{1}{4}}} \right) \right\}, \qquad (33)$$

where r_1, r_2 are the roots of the quadratic, in z^4, from the denominator of (32), $r_1 = -640 + 128\sqrt{5}$, $r_1 = -640 - 128\sqrt{5}$. Although the velocity gradients decay exponentially for large z, the approximation (32) predicts polynomial decay like z^{-8}. As the gradients in this regime are small the effect on the viscoelastic stress should be negligible. We can also investigate how well the weak-coupling assumption holds. The Padé approximation of the velocity field is compared to the finite element result in Fig. 6 for $\lambda = 0$, 0.1 and 0.2. For increasing λ there is a slight reduction in the velocity gradient, as streamlines are deflected from the stagnation point due to hoop-stresses, though this effect is small, even for $\mu_s = 0.5$. The Padé flow field does slightly underpredict the velocity field near the stagnation point, though generally it gives a good a prediction of the velocity field having only 0.2% error for large z.

4.1. Inversion of normal stress

The approximate model captures the behavior of the full numerical model for the components T_{11}, T_{22}. However, these components cannot be deduced directly from experiments. The first normal stress difference N_1 can be found from birefringence experiments. To $\mathcal{O}(\mu_p)$ this is given by

$$N_1 = 2\mu_s \left(u_{x_1}^{(0)} - v_{x_2}^{(0)}\right) + \mu_p \left(T_{11}^{(0)} - T_{22}^{(0)}\right) + 2\mu_s \mu_p \left(u_{x_1}^{(1)} - v_{x_2}^{(1)}\right).$$

It is helpful to note that the elastic stress components at the stagnation point can be written as

$$T_{11}^{(0)} = \frac{\pi U_0}{2h - \pi \lambda U_0}, \qquad T_{22}^{(0)} = -\frac{\pi U_0}{\pi \lambda U_0 + 2h}. \qquad (34)$$

We can see that the normal stress difference depends on the corrected velocity $\mathbf{u}^{(1)}$ through the Newtonian stress. For the sake of closure we will assume that the contribution from the elastic stress is larger than that from the Newtonian stress modified by the corrected velocity field.

Viscoelastic parameters are often found from fitting PDE simulations to the experimental data. As we now have an explicit expression for the normal stress difference along the center line of the channel, we can invert to obtain the fluid parameters (μ_p, λ) in terms of measurables quantities. The question is what physical measurables should we map the parameters to? The first normal stress difference at the stagnation point (N_{stag}) is readily observable and sensitive to the fluid parameters. For the second measurable quantity we will use the variance of the first normal stress difference along the center line (V_{ar}). Although the integral can be evaluated analytically by use of the residue theorem the result is transcendental. We thus expand the integral for small $U_0 \lambda / h$ and recover the expression

$$V_{ar} = 2 \int_0^\infty x^2 N_1 dx \sim \frac{U_0}{h} \left(6.35 \left(\mu_s + \mu_p\right) \right.$$
$$\left. + 10.79 \frac{U_0 \mu_p \lambda}{h} + 61.56 \mu_p \left(\frac{U_0 \lambda}{h}\right)^2 + \mathcal{O}\left(\left(\frac{U_0 \lambda}{h}\right)^3\right) \right). \qquad (35)$$
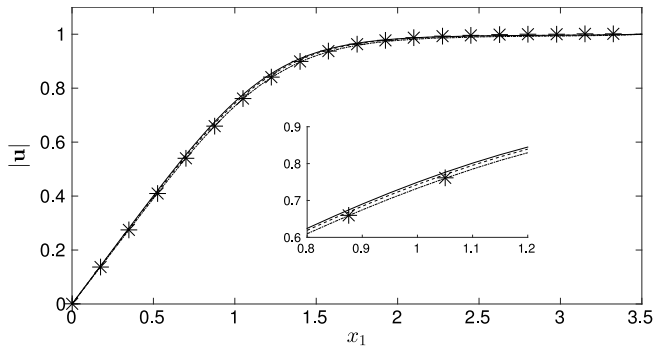
Fig. 6. The magnitude of the velocity along the center line. The numerical results for $\mu_p = 0.5$ and $\delta = 0.1$ for $\lambda = 0, 0.1$ and 0.2 are given by the solid, dashed and dot dashed lines respectively. The velocity given by the Padé approximation is given by asterisks.

Similarly, for small λ, the normal stress at the stagnation point is given by

$$N_{\text{stag}} = \frac{\pi U_0 \left(\mu_s + \mu_p \right)}{h} + \frac{\mu_p \pi^3 U_0^3 \lambda^2}{4h^3} + \mathcal{O}\left(\left(\frac{U_0 \lambda}{h} \right)^4 \right). \qquad (36)$$

We can invert by iteration to give:

$$\lambda \approx K - 45.88 \frac{h}{U} K^2 + \mathcal{O}\left(\left(\frac{U_0 \lambda}{h} \right)^3 \right), \qquad (37)$$

where R, K are given by

$$R = \frac{V_{ar} - \frac{6.43 \mu_s U_0}{h}}{N_{\text{stag}} - \frac{2\pi U_0 \mu_s}{h}}, \qquad K = \frac{h}{10.79 U_0} \left(R - 6.35 \right). \qquad (38)$$

Once λ is known the polymer viscosity can be easily found by inverting Eq. (36). Thus the viscoelastic parameters can be approximated given the variation and strength of the first normal stress difference around the stagnation point.

4.2. Second order fluid

Thus far we have used a weak-coupling limit to solve our system approximately. Alternatively we could have used the second order fluid (SOF) model to calculate the stresses, although this does not satisfy momentum conservation. In spite of this the solution for a SOF is purely algebraic and readily solved without approximation. Use of the relation $w'(z) = u_1 - iu_2$, along with the Cauchy–Riemann equations and the property that w and all of its derivatives are harmonic functions, allows one to construct all of the partial derivatives of the velocity field by considering, in turn, the real ($\Re$) and imaginary ($\Im$) parts of (24). Upon doing so, one can obtain Eqs. (39) and (40) for the normal stress components of the extra viscoelastic stress:

$$T_{11} = 2\mu \Re \left\{ w''(t) \right\} - 2W_e \mu \left(\Re \left\{ w'(t) \right\} \Re \left\{ w'''(z) \right\} \right.$$
$$\left. + \Im \left\{ w'(t) \right\} \Im \left\{ w''(t) \right\} \right)$$
$$+ 4W_e \mu \left(\Re\{ w''(t) \}^2 + \Im\{ w''(t) \}^2 \right), \qquad (39)$$

$$T_{22} = -2\mu \Re \left\{ w''(t) \right\} + 2W_e \mu \left(\Re \left\{ w'(t) \right\} \Re \left\{ w'''(t) \right\} \right.$$
$$\left. + \Im \left\{ w'(t) \right\} \Im \left\{ w'''(t) \right\} \right)$$
$$+ 4W_e \mu \left(\Re\{ w''(t) \}^2 + \Im\{ w''(t) \}^2 \right). \qquad (40)$$

We find that the discrepancy between the Hele–Shaw elongation rate and the FEM result at the stagnation point is of the order of 2% for an aspect ratio of $\delta = 0.1$. In Figs. 7 and 8, we can see that
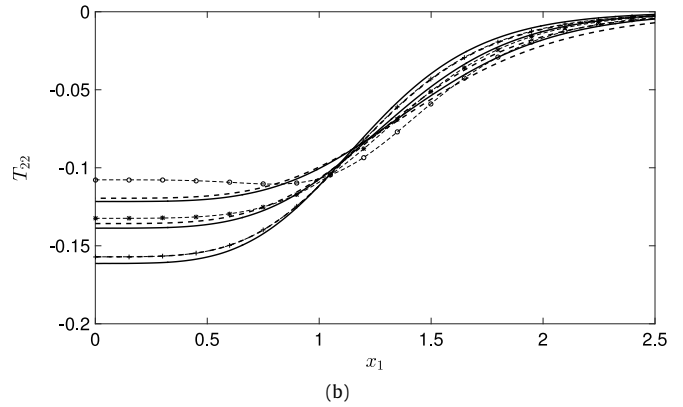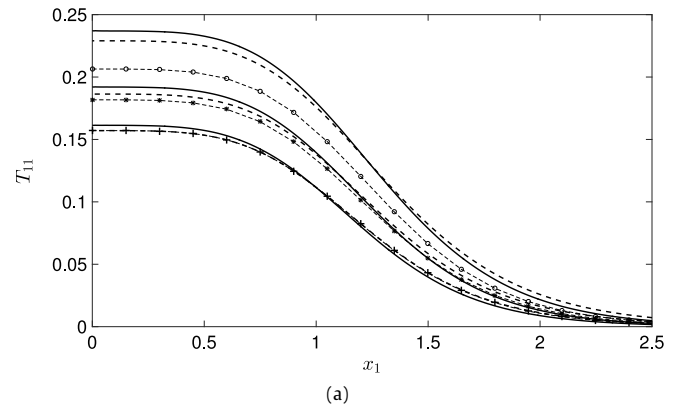

(a)

(b)

Fig. 7. Diagonal viscoelastic stress components with polymer viscosity $\mu_p = 0.1$ and $\delta = 0.1$, (a) T_{11}, (b) T_{22}. The crossed, dotted and circular marked lines denote the SOF solution whereas the solid and dashed lines denote the FEM Oldroyd B model and similarly the weak coupling Padé solution respectively. The curves are given for $W_e = 0, 0.1$ and 0.2, which go from bottom to top in (a), and top to bottom in (b).

the behavior predicted by the complex potential theory is similar to that predicted by the finite element model, however, the weak-coupling approach does significantly better. The small error in the velocity gradient can easily be attributed to non-zero δ. The effects of changing the aspect ratio at the stagnation point are shown in Fig. 9. This shows that in the limit of small δ, the FEM solution for $W_e = 0$ tends to the analytic solution. However, this is not true for non-zero W_e. This error is consistent with the use of a second order fluid model to approximate the Oldroyd B model. Even with an aspect ratio of $\delta = 0.05$ we find that the error is only 3% for $W_e = 0.1$. We note that the dependence at the stagnation point of the first normal stress difference on the Weissenberg number is of order W_e^2 and thus cannot be predicted by the second order fluid model as it is only accurate to order W_e. However it can be predicted from use of the weak coupling approximation.

5. Unequal inlet and outlet channel widths

We now consider the geometry of the cross-slot as before, but relax the condition that the widths of the inlet channel (h) and outlet channel (l) are equal. As the cross-slot geometry is commonly used in experimental studies due to the region of pure elongational flow, we will investigate the effect that changing the aspect ratio will have on the elongation rates and normal stresses. We define the ratio of outlet to inlet channel widths as $\alpha = h/l$. Then, by mass conservation it follows that $\alpha U_0 = U_{\text{out}}$, where U_0 and U_{out} are the inflow and outflow velocities respectively. Using the source term
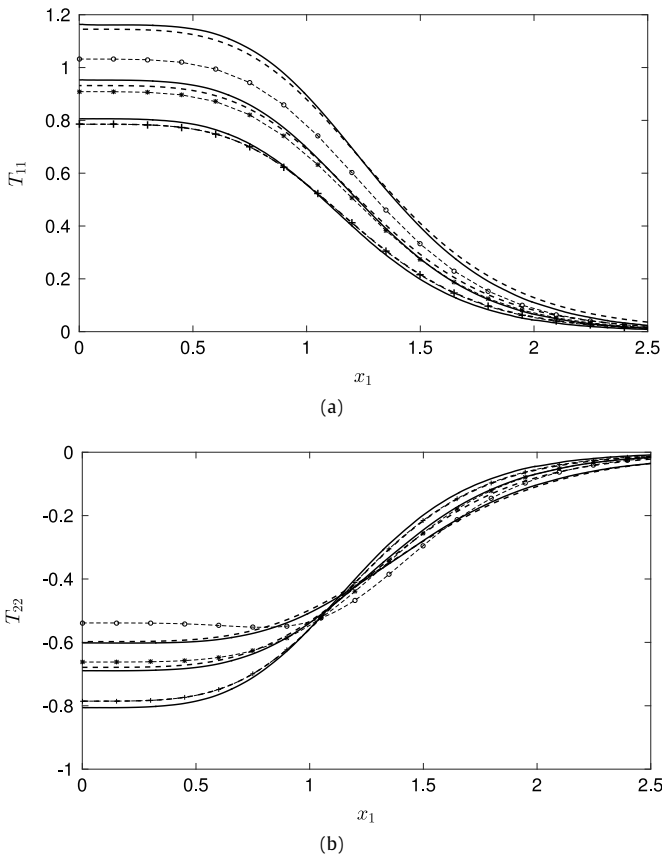
(a)

(b)

Fig. 8. Diagonal viscoelastic stress components with polymer viscosity $\mu_p = 0.5$ and $\delta = 0.1$, (a) T_{11}, (b) T_{22}. The crossed, dotted and circular marked lines denote the SOF solution whereas the solid and dashed lines denote the FEM Oldroyd B model and similarly the weak coupling Padé solution respectively. The curves are given for $W_e = 0$, 0.1 and 0.2, which go from bottom to top in (a), and top to bottom in (b).

as defined in Eq. (9), we can determine the boundary conditions at the outlet and inlet in the form:

$$\frac{dw}{dz} \sim -U_0 \alpha \quad \text{as} \quad \eta \to \pm\infty, \tag{41}$$

$$\frac{dw}{dz} \sim U_0 i \quad \text{as} \quad \eta \to 0. \tag{42}$$

This enables us to determine the constants in Eq. (6) to be $K = -\frac{h}{\alpha\pi}$, $b = \alpha^2$, $a = 1$. This leads to

$$\frac{dw}{dz} = -U_0 \alpha \sqrt{\frac{\eta + 1}{\eta - \alpha^2}}, \tag{43}$$

$$\frac{dz}{d\eta} = -\frac{h}{\alpha\pi} \eta^{-1}(\eta + 1)^{-\frac{1}{2}}(\eta - \alpha^2)^{\frac{1}{2}}. \tag{44}$$

Eq. (44) can be solved to give

$$z(\eta) = -\frac{h}{\alpha\pi} \ln\left(\frac{1}{2}(1 - \alpha^2) + \eta + \sqrt{(\eta + 1)}\sqrt{(\eta - \alpha^2)}\right)$$

$$+ \frac{hi}{2\pi} \ln\left(\left(-\alpha^2 i + \frac{1}{2}(1 - \alpha^2)i\eta + \sqrt{\eta + 1}\sqrt{\eta - \alpha^2}\right)^2\right)$$

$$- \frac{hi}{2\pi} \ln(\eta^2)$$

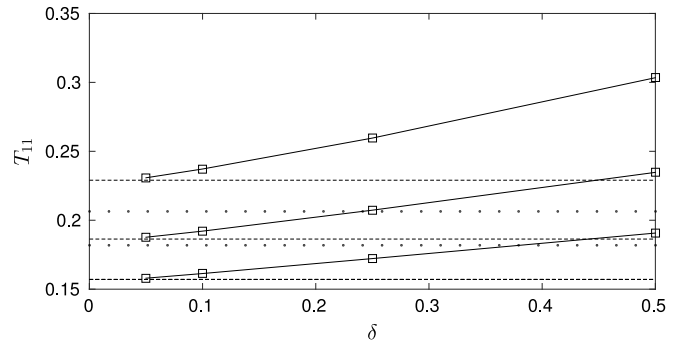$$+ \frac{h}{\alpha\pi}(1 - \alpha i) \ln(\alpha^2 + 1), \tag{45}$$

Fig. 9. T_{11} component of the extra stress at the stagnation point for $W_e = 0$ (bottom line), $W_e = 0.1$, $W_e = 0.2$ (top line) with $\mu_p = 0.1$ for varying δ. The Hele-Shaw ($\delta = 0$) solutions are given by horizontal dashed lines for the weak-coupling solution and the dotted line for the second order fluid approximation respectively.
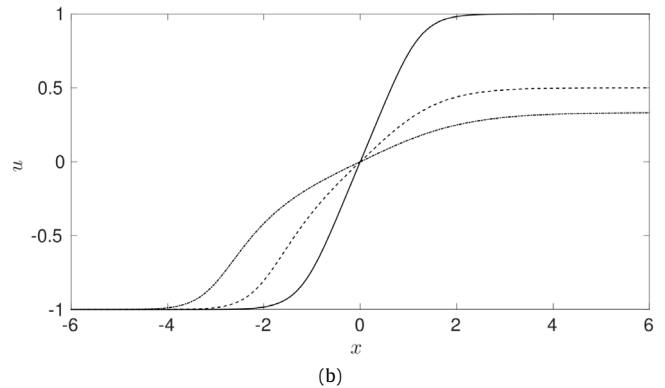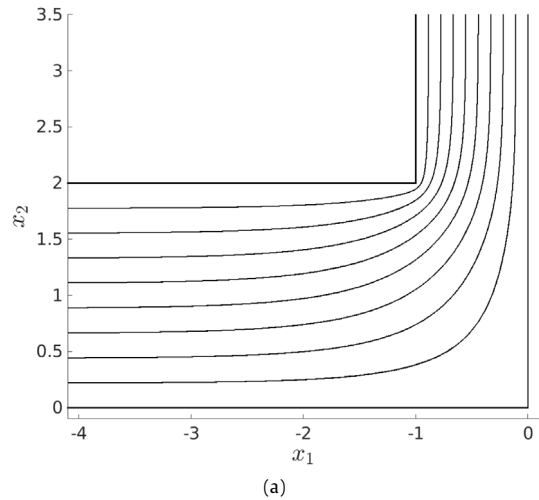

(a)

(b)

Fig. 10. (a) The streamlines for $\alpha = \frac{1}{2}$. (b) The velocity magnitude along the center line for $\alpha = 1, \frac{1}{2}, \frac{1}{3}$ which are denoted by the solid, dashed and dot-dashed lines respectively. The positive x values have the convention of being downstream of the stagnation point whilst the negative x values are upstream from the stagnation point.

where the constant is again assigned such that $z = 0$ at $\eta = -1$. Using a Newton–Raphson scheme to find $\eta(z)$, we can plot the streamlines and the velocity profiles along the center line (Fig. 10). The velocity gradients can be obtained from the equation

$$\frac{d^2 w}{dz^2} = -\frac{U_0 \alpha^2 \pi \eta (\alpha^2 + 1)}{2h(\eta - \alpha^2)^2}. \tag{46}$$
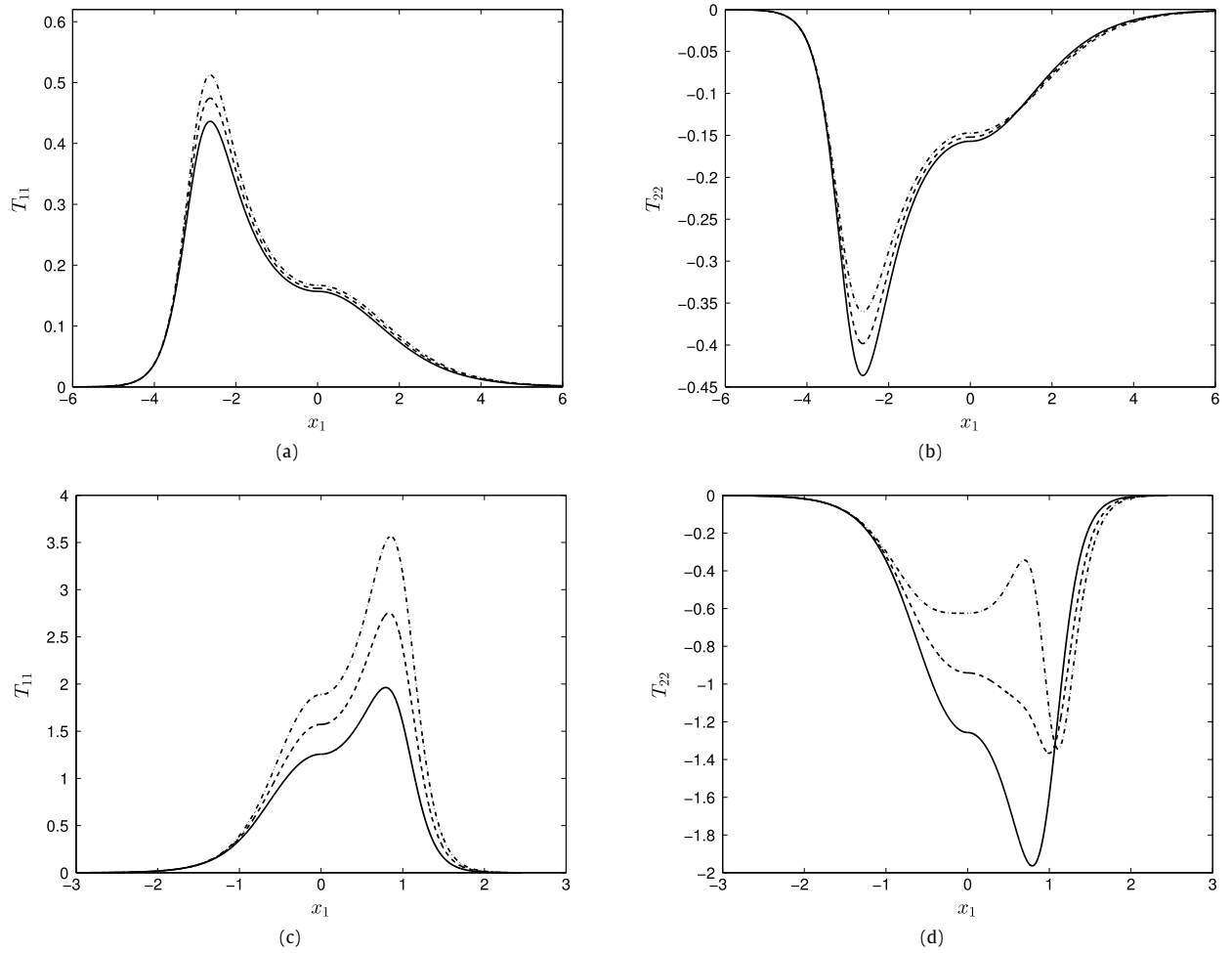
Fig. 11. The normal stress components for $\alpha = \frac{1}{3}$ are shown in (a) and (b) and those for $\alpha = 2$ are shown in (c) and (d). The polymer viscosity is taken to be $\mu_p = \frac{1}{2}$ and the results for $W_e = 0$, 0.1 and 0.2 are given by the solid, dashed and dot-dashed lines respectively.

Evaluating the above equation at the stagnation point gives a simple expression for the elongation rate for a given aspect ratio,

$$\dot{\varepsilon}_{stag} = \frac{U_0\pi\alpha^2}{2h(1+\alpha^2)}. \tag{47}$$

We can thus expect the elongation rate to behave as α^2 for small α. We also obtain the result that the maximum elongation rate achievable at the stagnation point for potential flow is $\frac{U_0\pi}{2h}$. One might have expected the maximum elongation to become singular as the outlet channel is contracted, as the flow is being forced into an infinitely small contraction. This rather surprising result can be explained by observing that although the elongation rate does become singular, the maximum value does not occur at the stagnation point. For $\alpha > 1$ the maximum value occurs downstream of the stagnation point and for $\alpha < 1$ the maximum occurs upstream. From Eq. (46) we can see that the maximum occurs when $\eta = -\alpha^2$. When $\alpha = 1$, by the choice of mapping in (5), the location of maximum elongation rate coincides with the stagnation point. We can thus find the maximum elongation rate by substituting $\eta = -\alpha^2$ into Eq. (46) to give

$$\dot{\varepsilon}_{max} = \frac{U_0\pi\left(\alpha^2+1\right)}{8h}, \tag{48}$$

where, in this case, the elongation rate does become singular as $\alpha \to \infty$ as expected.

For the asymmetric system we chose not to use the weak-coupling approach. Although in the previous section it was shown

to be superior to the SOF approach, the requirement for the Padé approximation to capture the asymmetry leads to rather cumbersome expressions for the stresses T_{11}, T_{12}. Instead we introduce the effect of viscoelasticity by using the SOF approach, by using Eqs. (39) and (40) to model the normal stress. The results are given in Fig. 11. The elongation rate can be deduced from the Newtonian case, and it can be seen that the maximum elongation occurs upstream for $\alpha < 1$ and downstream for $\alpha > 1$. One can also see that viscoelasticity has a much smaller effect for $\alpha < 1$ due to the much smaller velocity gradients. Downstream of the stagnation point these effects are negligible. Using the exact elongation rate gives normal stress components as:

$$T_{11} = \frac{U_0\mu\pi\alpha^2}{(1+\alpha^2)h} + \frac{W_e\mu U_0^2\pi^2\alpha^4}{(1+\alpha^2)h^2},$$

$$T_{22} = -\frac{U_0\mu\pi\alpha^2}{(1+\alpha^2)h} + \frac{W_e\mu U_0^2\pi^2\alpha^4}{(1+\alpha^2)h^2}.$$

Having derived an analytical velocity field we now consider whether or not greater uniformity of the elongation rate along the channel can be achieved by simply changing the aspect ratio. This is of key importance for extensional flow studies. Let us suppose that we wish to achieve a fixed elongation rate $\dot{\varepsilon}_0$ at the stagnation point, which, by Eq. (47), forces the condition $\frac{U_0\pi}{2h} = \frac{1+\alpha^2}{\alpha^2}\dot{\varepsilon}_0$. We now scale z by the inlet width h/π and w'' by $\dot{\varepsilon}_0$. The total curvature of the velocity field, S, is used as a metric for the uniformity of the

elongation rate

$$S = \int_C |\kappa(z)| dz = \int_{-\infty}^{0} \left| \frac{w'''}{\left(1 + w''^2\right)^{\frac{3}{2}}} \right| \frac{dz}{d\eta} d\eta, \qquad (49)$$

where C is a contour traversing the center line which is readily converted into a real integral by using the mapping (5). Evaluation of the above integral leads to the expression

$$S = \frac{2\left(1 + \alpha^2\right)^2}{\sqrt{\alpha^8 + 4\alpha^6 + 22\alpha^4 + \alpha^2 + 1}}. \qquad (50)$$

S has a minimum value when $\alpha = 1$. Thus greater uniformity cannot be achieved by simply changing inlet–outlet aspect ratios.

6. Conclusions

We have derived the Hele–Shaw flow solution for a two-dimensional cross-slot device. The principle result of the paper is that the viscoelastic normal stresses derived using weak-coupling theory can be used to predict behavior that is shown to accurately reproduce the stress to match that computed from a fully coupled numerical model. This leads to an expression for the stresses which accurately reproduces the diagonal stress components. The viscoelastic parameters can then be expressed in terms of the peak and spread of the first normal-stress difference. The results were generalized to give an explicit solution for the normal stresses at the stagnation point for inlet and outlet channels of different widths.

Acknowledgments

References

[1] P.J. Oliveira, An exact solution for tube and slit flow of a FENE-P fluid, Acta Mech. 158 (3–4) (2002) 157–167.

[2] K.R. Rajagopal, R.K. Bhatnagar, Exact solutions for some simple flows of an Oldroyd-B fluid, Acta Mech. 113 (1995) 233–239.

[3] S. Drost, J. Westerweel, Hele–Shaw rheometry, J. Rheol. 57 (6) (2013) 1787–1801.

[4] P. Fast, L. Kondic, M.J. Shelley, P. Palffy-Muhoray, Pattern formation in non-Newtonian Hele–Shaw flow, Phys. Fluids 13 (5) (2001) 1191–1212.

[5] G.W.M. Peters, J.F.M. Schoonen, F.P.T. Baaijens, H.E.H. Meijer, On the performance of enhanced constitutive models for polymer melts in a cross-slot flow, J. Non-Newton. Fluid Mech. 82 (1999) 387–427.

[6] J. Soulages, T. Schweizer, D.C. Venerus, J. Hostettler, F. Mettler, M. Kröger, H.C. Öttinger, Lubricated optical rheometer for the study of two-dimensional complex flows of polymer melts, J. Non-Newton. Fluid Mech. 150 (1) (2008) 43–55.

[7] A. Abedijaberi, J. Soulages, M. Kröger, B. Khomami, Flow of branched polymer melts in a lubricated cross-slot channel: a combined computational and experimental study, Rheol. Acta 48 (1) (2009) 97–108.

[8] D.D. Joseph, T. Funada, J. Wang, Potential Flows of Viscous and Viscoelastic Fluids, Cambridge University Press, New York, 2007.

[9] D.D. Joseph, Bernoulli equation and the competition of elastic and inertial pressures in the potential flow of a second-order fluid, J. Non-Newton. Fluid Mech. 42 (3) (1992) 385–389.

[10] S.J. Haward, M. Oliveira, M.A. Alves, G.H. McKinley, Optimized cross-slot flow geometry for microfluidic extensional rheometry, Phys. Rev. Lett. 109 (2012) 128–301.

[11] K.D. Coventry, M.R. Mackley, Cross-slot extensional flow birefringence observations of polymer melts using a multi-pass rheometer, J. Rheol. 52 (2) (2008) 401–415.

[12] D.G. Hassell, D. Auhl, T.C.B. McLeish, M.R. Mackley, The effect of viscoelasticity on stress fields within polyethylene melt flow for a cross-slot and contraction-expansion slit geometry, Rheol. Acta 47 (7) (2008) 821–834.

[13] G.N. Rocha, R.J. Poole, M.A. Alves, P.J. Oliveira, On extensibility effects in the cross-slot flow bifurcation, J. Non-Newton. Fluid Mech. 156 (1–2) (2009) 58–69.

[14] P.C. Sousa, F.T. Pinho, M.S.N. Oliveira, M.A. Alves, Purely elastic flow instabilities in microscale cross-slot devices, Soft Matter 11 (2015) 8856–8862.

[15] F.A. Cruz, R.J. Poole, A.M. Afonso, F.T. Pinho, P.J. Oliveira, M.A. Alves, Influence of channel aspect ratio on the onset of purely-elastic flow instabilities in three-dimensional planar cross-slots, J. Non-Newton. Fluid Mech. 227 (Supplement C) (2016) 65–79.

[16] R.J. Poole, G.N. Rocha, P.J. Oliveira, A symmetry-breaking inertial bifurcation in a cross-slot flow, Comput. Fluids 93 (2014) 91–99.

[17] D.O.A. Cruz, F.T. Pinho, Analytical solution of steady 2d wall-free extensional flows of UCM fluids, J. Non-Newton. Fluid Mech. 223 (Supplement C) (2015) 157–164.

[18] B. Thomases, M. Shelley, Emergence of singular structures in Oldroyd-B fluids, Phys. Fluids 19 (10) (2007).

[19] M. Renardy, A comment on smoothness of viscoelastic stresses, J. Non-Newton. Fluid Mech. 138 (2) (2006) 204–205.

[20] P. Becherer, A.N. Morozov, W. van Saarloos, Scaling of singular structures in extensional flow of dilute polymer solutions, J. Non-Newton. Fluid Mech. 153 (2) (2008) 183–190.

[21] P. Becherer, W. van Saarloos, A.N. Morozov, Stress singularities and the formation of birefringent strands in stagnation flows of dilute polymer solutions, J. Non-Newton. Fluid Mech. 157 (1) (2009) 126–132.

[22] M. Renardy, A matched solution for corner flow of the upper convected Maxwell fluid, J. Non-Newton. Fluid Mech. 58 (1) (1995) 83–89.

[23] J.M. Rallison, E.J. Hinch, The flow of an Oldroyd fluid past a reentrant corner: the downstream boundary layer, J. Non-Newton. Fluid Mech. 116 (2–3) (2004) 141–162.

[24] J.D. Evans, Re-entrant corner flows of the upper convected Maxwell fluid, Proc. Math. Phys. Eng. Sci. 461 (2053) (2005) 117–142.

[25] R. Keunings, On the high Weissenberg number problem, J. Non-Newton. Fluid Mech. 20 (1986) 209–226.

[26] P. Singh, L.G. Leal, Finite element simulation of flow around a $\frac{3\pi}{2}$ corner using the FENE dumbbell model, J. Non-Newton. Fluid Mech. 58 (2–3) (1995) 279–313.

[27] G.K. Batchelor, An Introduction to Fluid Mechanics, Cambridge University Press, Massachusetts, 1967.

[28] L.M. Milne-Thomson, Theoretical Hydrodynamics, Macmillan, London, 1962.

[29] J.M. Rallison, E.J. Hinch, Do we understand the physics in the constitutive equation? J. Non-Newton. Fluid Mech. 29 (1988) 37–55.

[30] M. Behr, D. Arora, M. Pasquali, Stabilized Finite Element Methods of GLS Type for Oldroyd-B Viscoelastic Fluid, ECCOMAS, Jyväskylä, Finland, 2004.

[31] D.F. James, Boger fluids, Annu. Rev. Fluid Mech. 41 (1) (2009) 129–142.

[32] T.J. Craven, J.M. Rees, W.B.J. Zimmerman, Stablilized finite element modelling of Oldroyd-B viscoelastic flow, in: COMSOL User Conference 2006, Birmingham, 2006.

[33] T.J.R. Hughes, L.P. Franca, G.M. Hulbert, A new finite element formulation for computational fluid dynamics: VIII. The Galerkin/least-squares method for advective-diffusive equations, Comput. Methods Appl. Mech. Engrg. 73 (2) (1989) 173–189.

[34] M. Behr, D. Arora, O. Coronado, M. Pasquali, Stablilized finite element modelling of Oldroyd-B viscoelastic flow, in: Proc. of the Third MIT Conference on Computational Fluid and Solid Mechanics, Massachusetts Institute of Technology, Cambridge, USA, 2005, pp. 135–308.

[35] R.I. Tanner, Plane creeping flows of incompressible secondorder fluids, Phys. Fluids 9 (6) (1966) 1246–1247.

[36] M.N.J. Moore, M.J. Shelley, A weak-coupling expansion for viscoelastic fluids applied to dynamic settling of a body, J. Non-Newton. Fluid Mech. 183–184 (0) (2012) 25–36.